nature portfolio

https://doi.org/10.1038/s41563-022-01333-y

Supplementary information

Polymorphism of garnet solid electrolytes and its implications for grain-level chemo-mechanics

In the format provided by the authors and unedited

Supporting Information: Polymorphism of Garnet Solid Electrolytes and Its Implications on Grain Level Chemo-Mechanics

Marm B. Dixit [*†‡] Bairav S. Vishugopi[§] Wahid Zaman [†¶]
Peter Kenesei[‖] Jun-Sang Park[‖] Jonathan Almer[‖]
Partha Mukherjee[§] Kelsey B. Hatzell [*¶**]

[*]Lead Contact and Corresponding Author: kelsey.hatzell@princeton.edu and dixitmb@ornl.gov
[†]Department of Mechanical Engineering, Vanderbilt University, Nashville, TN, 37240, USA
[‡]Electrification and Energy Infrastructures Division, Oak Ridge National Laboratory, Oak Ridge, TN, 37830, USA
[§]School of Mechanical Engineering, Purdue University, West Lafayette, IN, USA, 47907
[¶]Department of Mechanical and Aerospace Engineering, Princeton University, Princeton, NJ, 08540, USA
[‖]Advanced Photon Source, Argonne National Laboratory, Lemont, IL 60439, USA
[**]Andlinger Center for Energy and the Environment, Princeton University, Princeton, NJ, 08540, USA

Contents

1 Supplemental Experimental Procedures

1.1 Data Analysis

Grains were indexed from the FF-HEDM data using the fourth through seventh Debye-Scherrer rings corresponding to the {231}, {040}, {240} and {332} lattice planes. The inner rings were avoided for indexing as they were attenuated by filters to reduce saturation of the detector. This also enables to acquire higher intensity on the low d-spacing outer rings to enable high strain resolution. Calibration, reconstruction and indexing was carrying out using the Microstructural Imaging and Diffraction Analysis Software (MIDAS). Reconstruction of the FF-HEDM data yielded the grain centroid position, grain averaged orientation and an elastic strain tensor. Grain identification is carried out by a procedure called indexing which is described here (Fig. S2). Starting with a diffraction spot, its position with respect to the ideal diffraction ring for grains positioned at (0, 0, 0) lab is calculated. A number of different combinations of centre-of-mass position and orientation of the diffracting grain can give rise to this observed position of the diffraction spot. This results in a number of possible positions of the diffracting grain, each with a different orientation of the diffracting plane normal and each of which can give rise to the observed diffraction spot but which, if placed at (0, 0, 0)lab, would result in a diffraction spot at one of the points on the ideal diffraction ring. Now, considering one of these points, the diffracting grain (with a fixed orientation of the diffracting plane normal) can be located not only at this point but at any position along the diffracted ray passing through this point and the observed diffraction spot. The combination of all these positions in the sample lying on diffracted rays to the observed diffraction spot and passing through the points found on the plane AA_0 defines a surface. The surface thus calculated is divided into a grid, and diffraction spots for all combinations of positions on the grid and orientations (by rotating the diffracting plane about its normal) are simulated and matched with the observed diffraction spots, using margins for the position on the detector, the position in and the volume of the grain. The combination of position and orientation with the best match is regarded as belonging to the grain in question. The criteria for estimating closeness of simulated and observed reflection is called completeness, which is a measure of grain tracking through the full sample rotation. Minimum completeness threshold is set at 70% for the reconstruction. Typical resolution for centroid positions is approximately 20 μm, angular position is 0.1 $^\circ$ and lattice strain resolution is 1E-4. Approximately 31000 grains were identified in a single pellet and are consistent across each measurement. The lattice strains are calculated based on the distortion of the crystal lattice from the reference crystal lattice spacing. For each grain, FF-HEDM can simultaneously track the elastic strain as a perturbation of the local lattice. Strain is computed as the difference in lattice parameters of an unstrained lattice to a strained lattice (Fig. **??**a, Sx). The direct space metric tensor, is a method of measuring distances in non-cartesian coordinate system. For an typical lattice, the direct space metric tensor is

given as,

$$A = \begin{pmatrix} a & bcos(\gamma) & ccos(\beta) \\ 0 & bsin(\gamma) & -csin(\beta)cos(\alpha^*) \\ 0 & 0 & csin(\beta)sin(\alpha^*) \end{pmatrix} \quad (1)$$

Where, (a,b,c,α,β,γ) and (a*,b*,c*,α^*,β^*,γ^*) are the direct and reciprocal space lattice parameters. The linear Langrangian strain tensor equation defines the strain for the lattice as follows:

$$\epsilon_{ij} = \frac{1}{2}(AA_0^-1 + A_0^-1A) - I \quad (2)$$

Where A and A_0 are the direct space metric tensors for strained and unstrained lattice respectively while I is an identity matrix. The lattice parameters are estimated during indexing routines to identify grain locations and orientations. This information is subsequently used with the formulation described here to estimate the elastic strain development in the grains. For the purposes of this study, the hydrostatic stress is typically reported as a grain-averaged quantity. Grain tracking between individual measurements is carried out by one-to-one correspondence of minimal distances between grain sets. All analysis of grain neighborhoods is carried out on the tracked data-sets enabling a direct spatial correlation between different measurements. In addition to spatial correlation between successive HEDM measurements, grain sets were also registered with corresponding tomography dataset using bounding dimensions as the registration metrics. All data analysis tasks are performed using custom-built routines in MATLAB. Specifically, k-means clustering (k=3) was used to identify spatial correlation between strain evolution during electrochemical cycling. Strain relaxation pathways are identified on cluster-averaged data by identifying location of steepest gradient from an identified location. The relaxation pathways are concluded when a local minima is reached. A local minima in this case refers to a grain neighborhood pair that show highest strain gradient when defined from either neighborhood.

1.2 Experimental set up and data

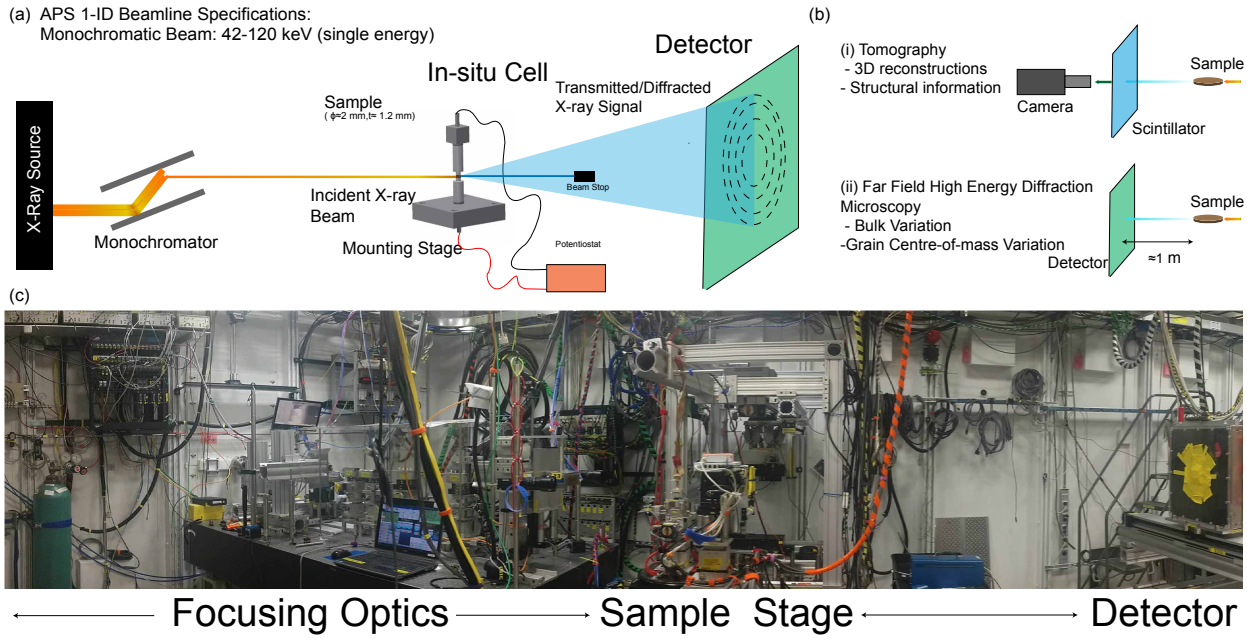

Fig S 1: Far field and tomography Measurement Experimental Setup. (a) Schematic diagram showing experimental setup with the relevant equipments highlighted. (b) End-station detectors for carrying out tomography and far-field high enregy diffraction microscopy measurements with the corresponding information expected. (c) Photograph of the experimental end-station at the Advanced Photon Source, 1-ID-E end station. The beam enters the hutch and passes through the end-station focusing optics before being incident on the sample. The diffracted signal are captured on a large area detector.

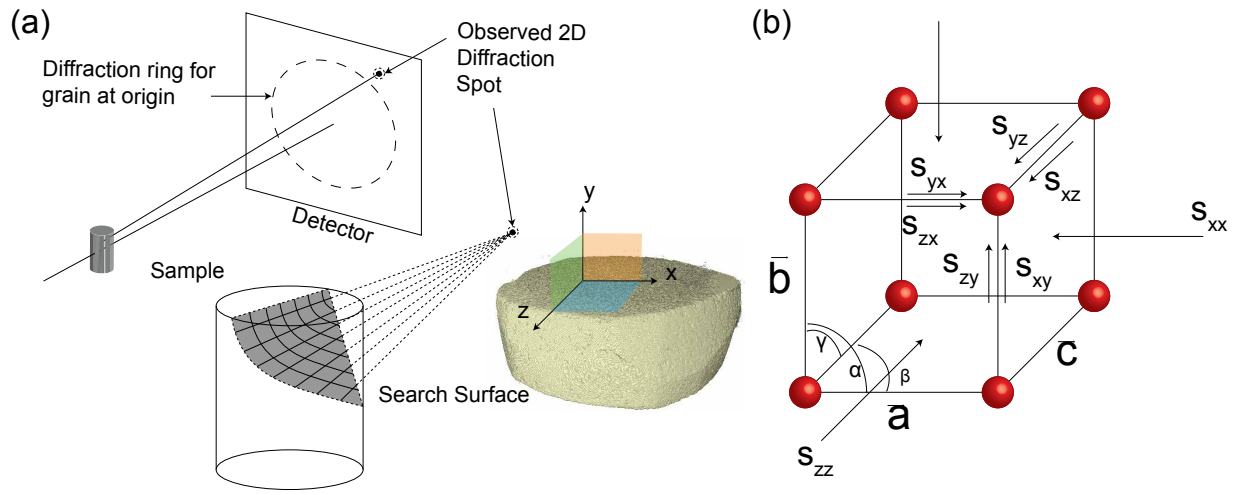

Fig S 2: Indexing process and data reduction for FF-HEDM. (a) Schematic diagram explaining indexing method for identifying grain orientation and COM. (b)Nomenclature for the strain tensor and correlation of the spatial co-ordinates with geometry.

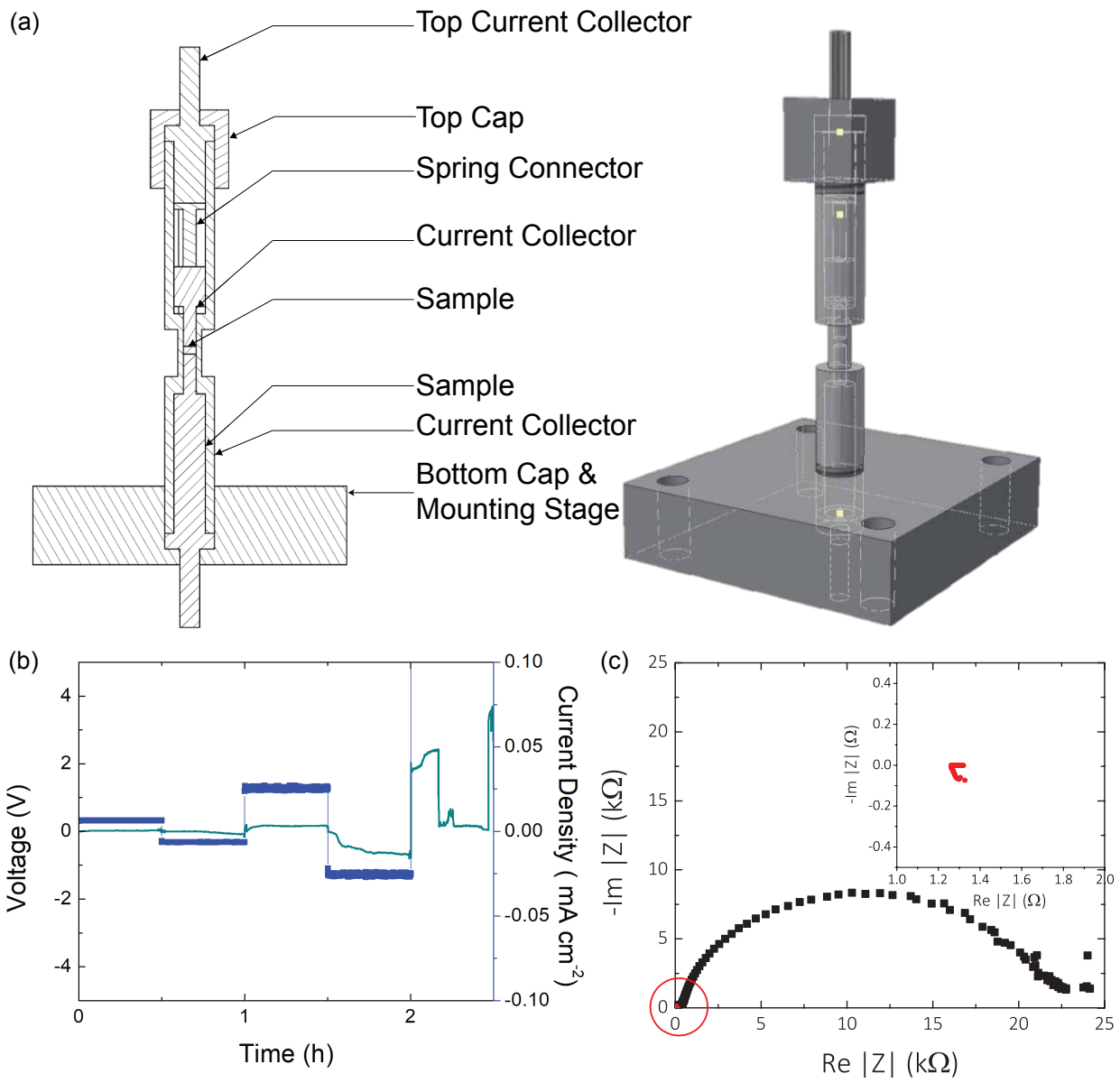

Fig S 3: *In situ* electrochemical measurements. (a) Schematic diagram showing the construction of an air sensitive cell for carrying out *in situ* experiments at the beamline. (b) Polarization profiles for plating and stripping measured on Li | LLZO | Li cells. A total of 1.5 mAh cm^{-2} lithium is cycled before failure. (c) Impedance measurements of the pristine and the failed cell(inset).

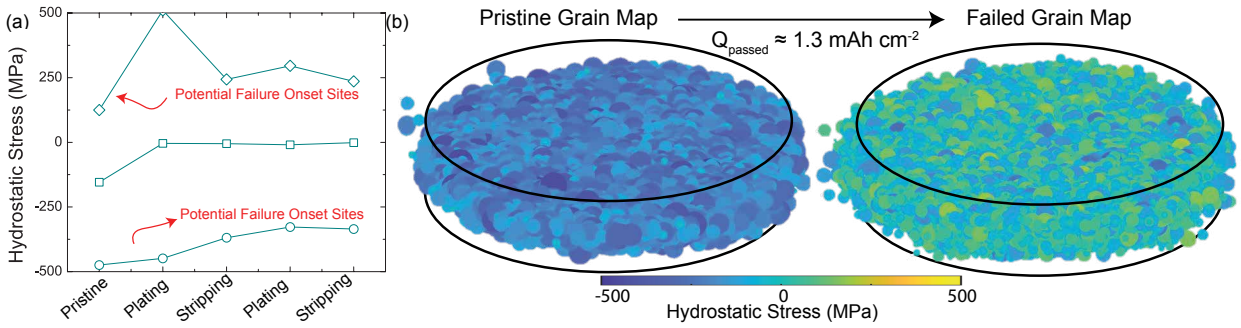

Fig S 4: Strain Response of Poly-crystalline LLZO Material for additional sample. (a)Hydrostatic stress evolution during cycling of Li|LLZO|Li sample. The stress values are averaged over all the grains in the measured sample. Maximum and minimum values are shown for individual grains in the sample. (d) 3D grain maps for pristine and failed sample with the grains color mapped to the stress values. A total of 1.3 mAh cm^{-2} lithium is cycled before failure.

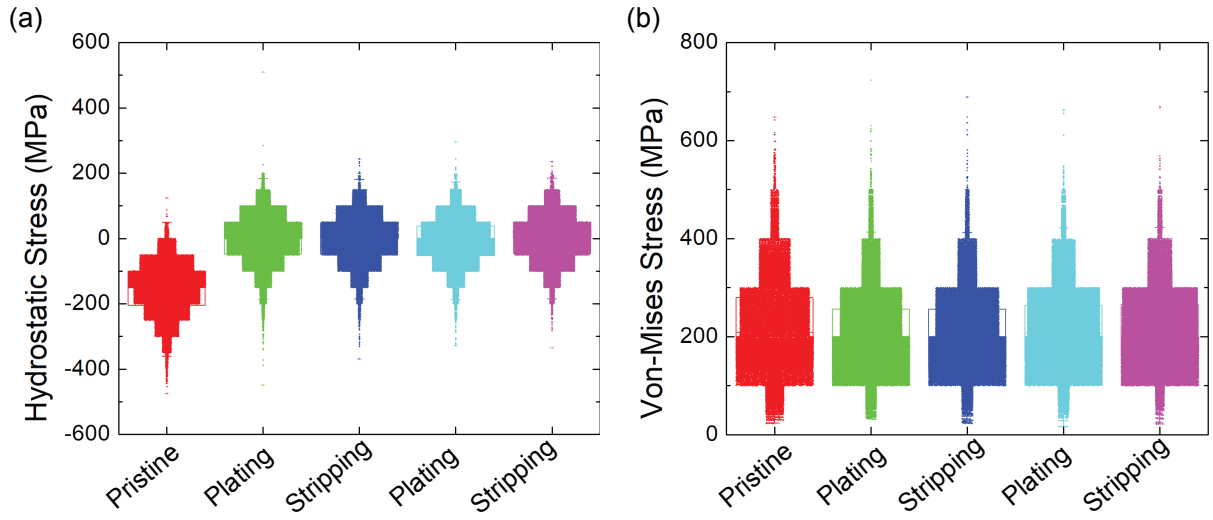

Fig S 5: Stress Response of Poly-crystalline LLZO Material. Violin plots depicting the overall stress distribution along with the individual data sets for hydrostatic (a,c) stress and Von-Mises stress (b,d) for additional sample. The width of the violin plots indicate the number density of grains at the specified stress value.

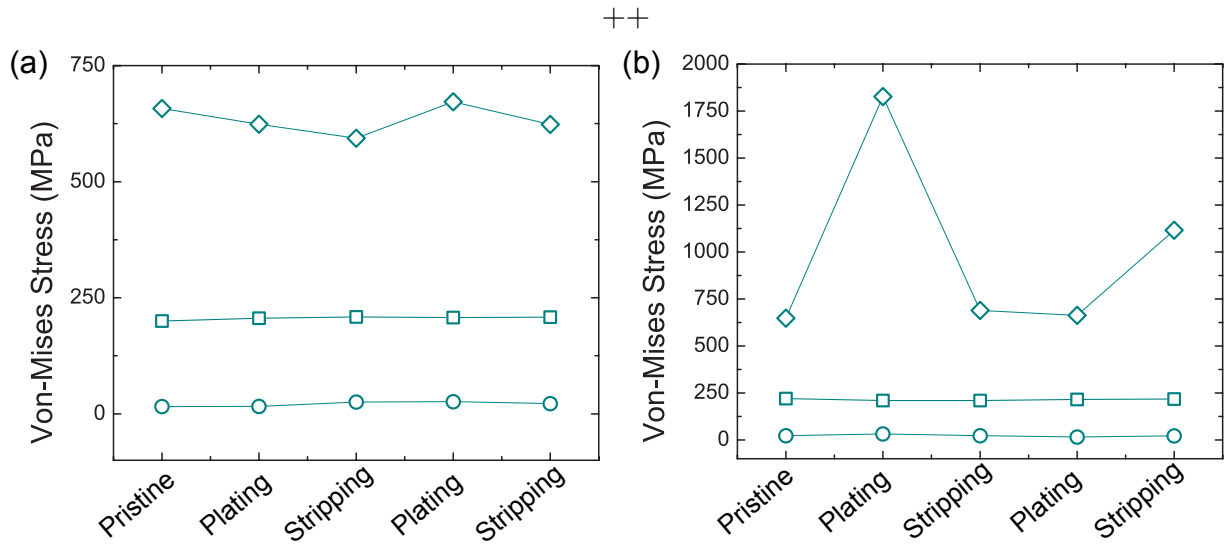

Fig S 6: Stress Response of Poly-crystalline LLZO Material. Von-Mises stress mapped over multiple electrochemical cycling for two samples measured (a-b).

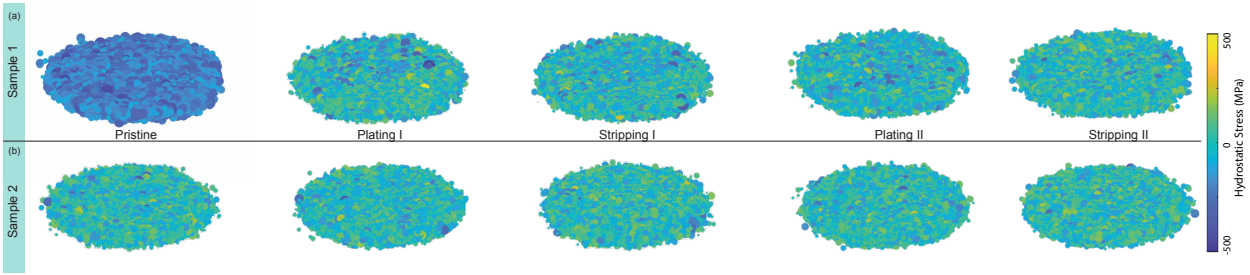

Fig S 7: Grain Maps for all the steps for two samples (a-b). The color mapping represents the hydrostatic stress for individual grains.

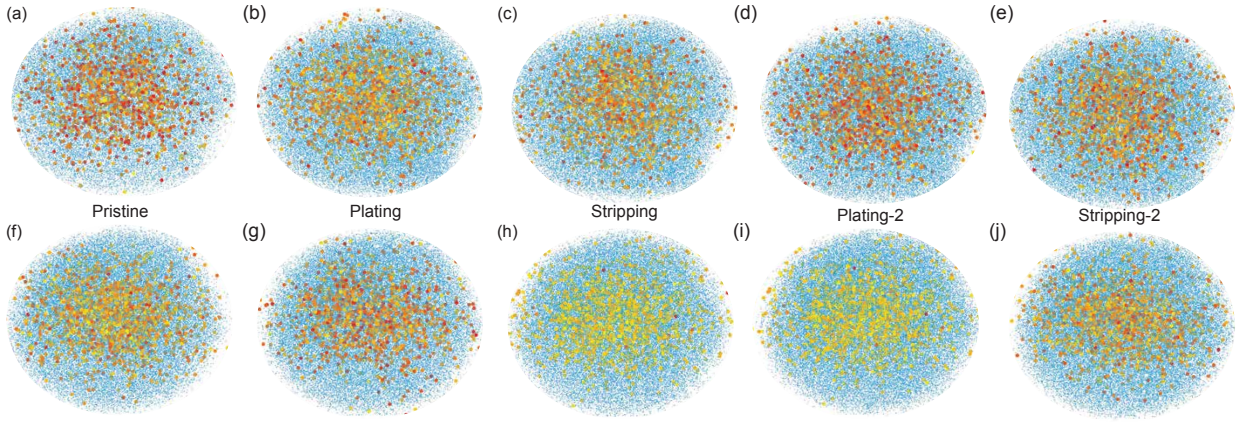

Fig S 8: Superposition maps for 220 SG grains (light blue) and 230 SG grains (larger scatter points, color mapped to stress state) for sample 1 (a-e) and sample 2 (f-j) at various states of electrochemical cycling.

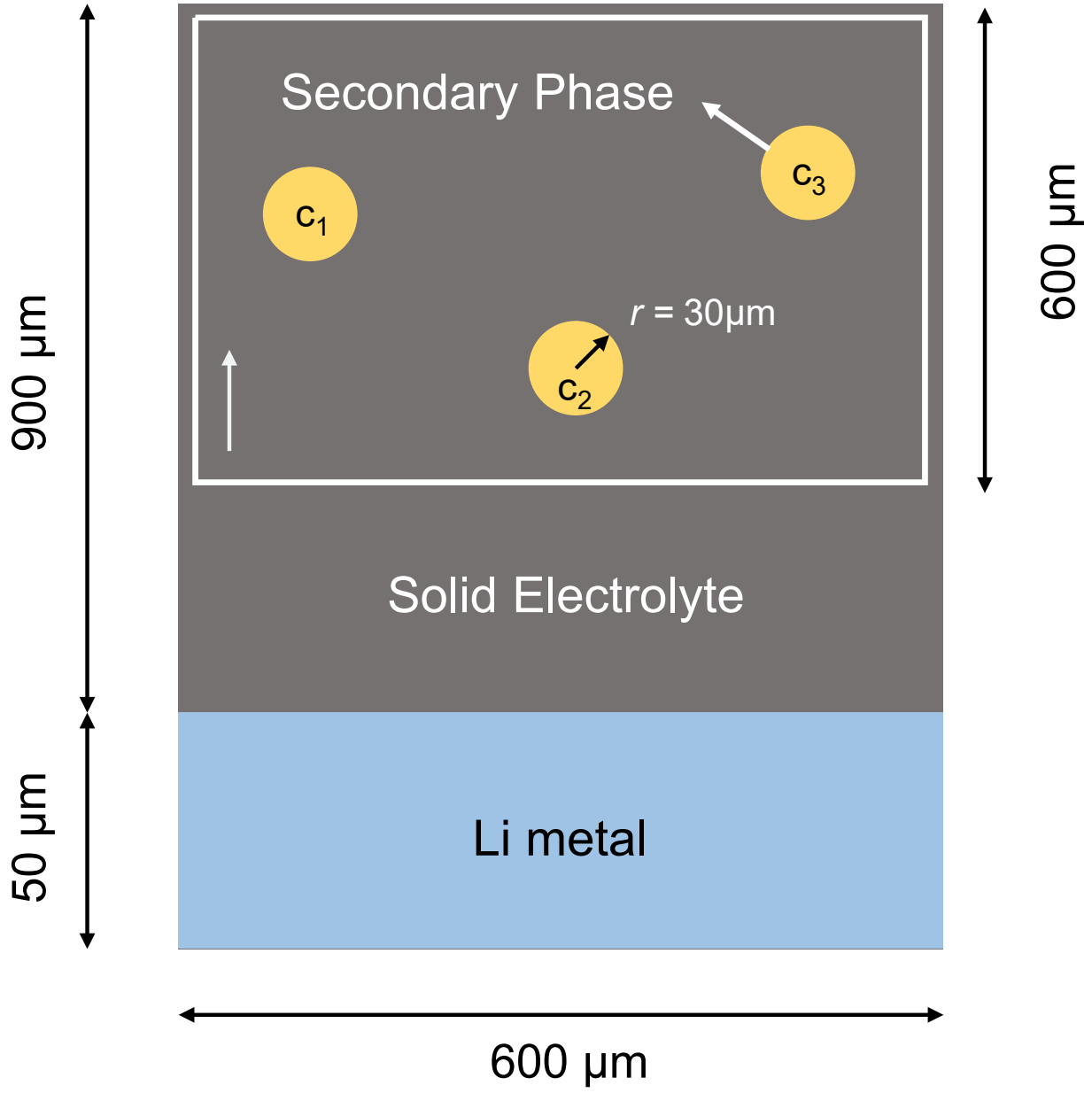

Fig S 9: Schematic showing the simulation domain used for the mesoscale modeling of electrochemical and mechanical response of LLZO with the secondary phases.

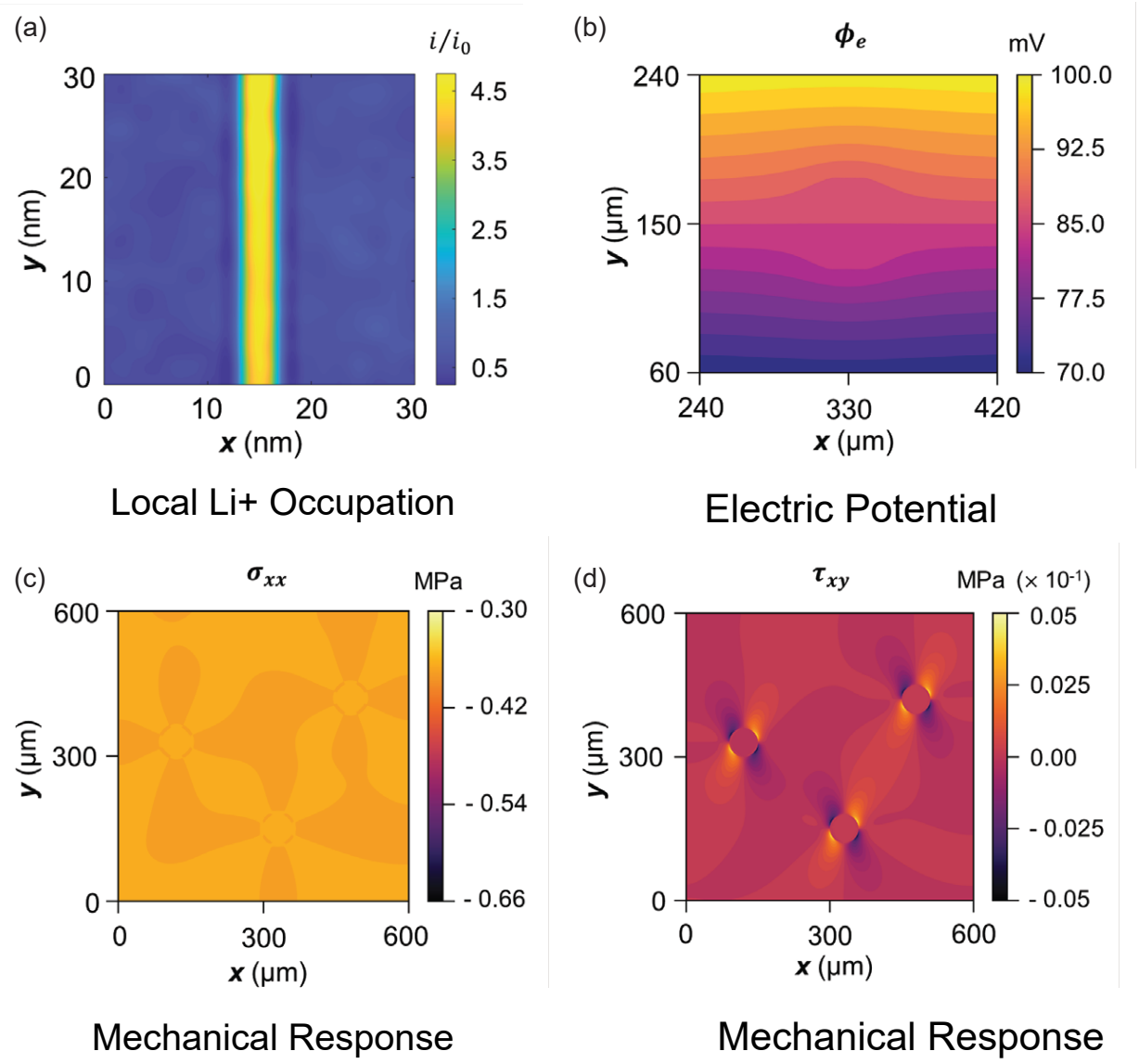

Fig S 10: Additional Modeling Results. (a) Mesoscale modeling results, highlighting the variation in local Li+ occupation due to the presence of the secondary phase, with a differing ion migration barrier when compared to the bulk. Here, the ion migration barrier in the secondary phase is 0.06 eV less than the bulk, which is in contrast to the case presented in the manuscript. (b) Electric potential distribution near the secondary phase. The ionic conductivities of the secondary phase and bulk are 1 mS cm^{-1} and 0.3 mS cm^{-1} respectively (this is in contrast to the case presented in the manuscript). (c-d) Mechanical stress distribution (x-direction and shear stress) in the solid electrolyte domain with the secondary phases.

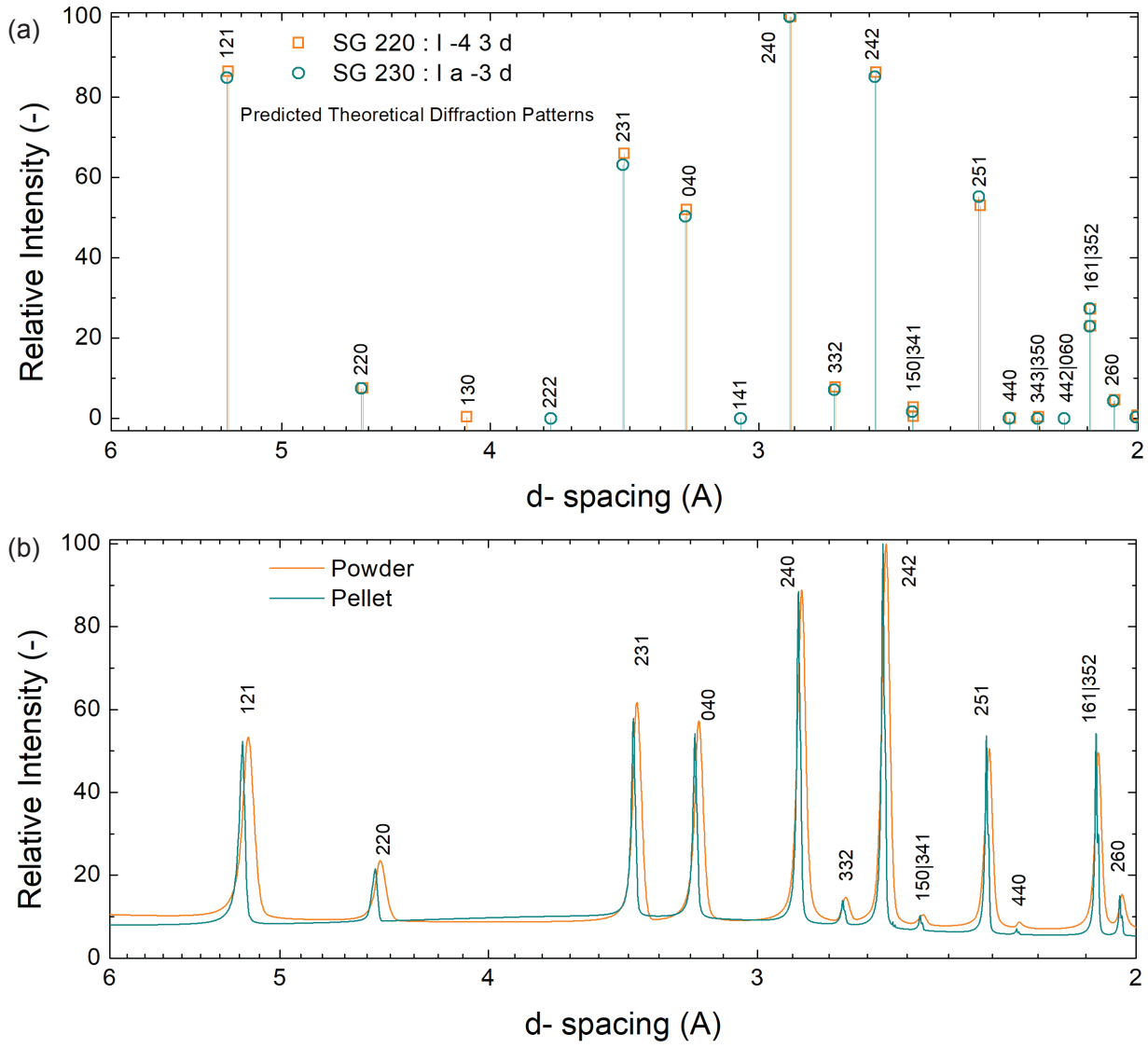

Fig S 11: Theoretical and laboratory XRD patterns for LLZO. (a) Theoretical XRD patterns for 220 and 230 sg. LLZO with corresponding <hkl> values mentioned. The only distinct reflections between the 220 and 230 sg. have low structure factors. (b) Laboratory XRD patterns of LLZO powder and pellet material. No evidence of the low structure factor reflections are observed in these patterns.

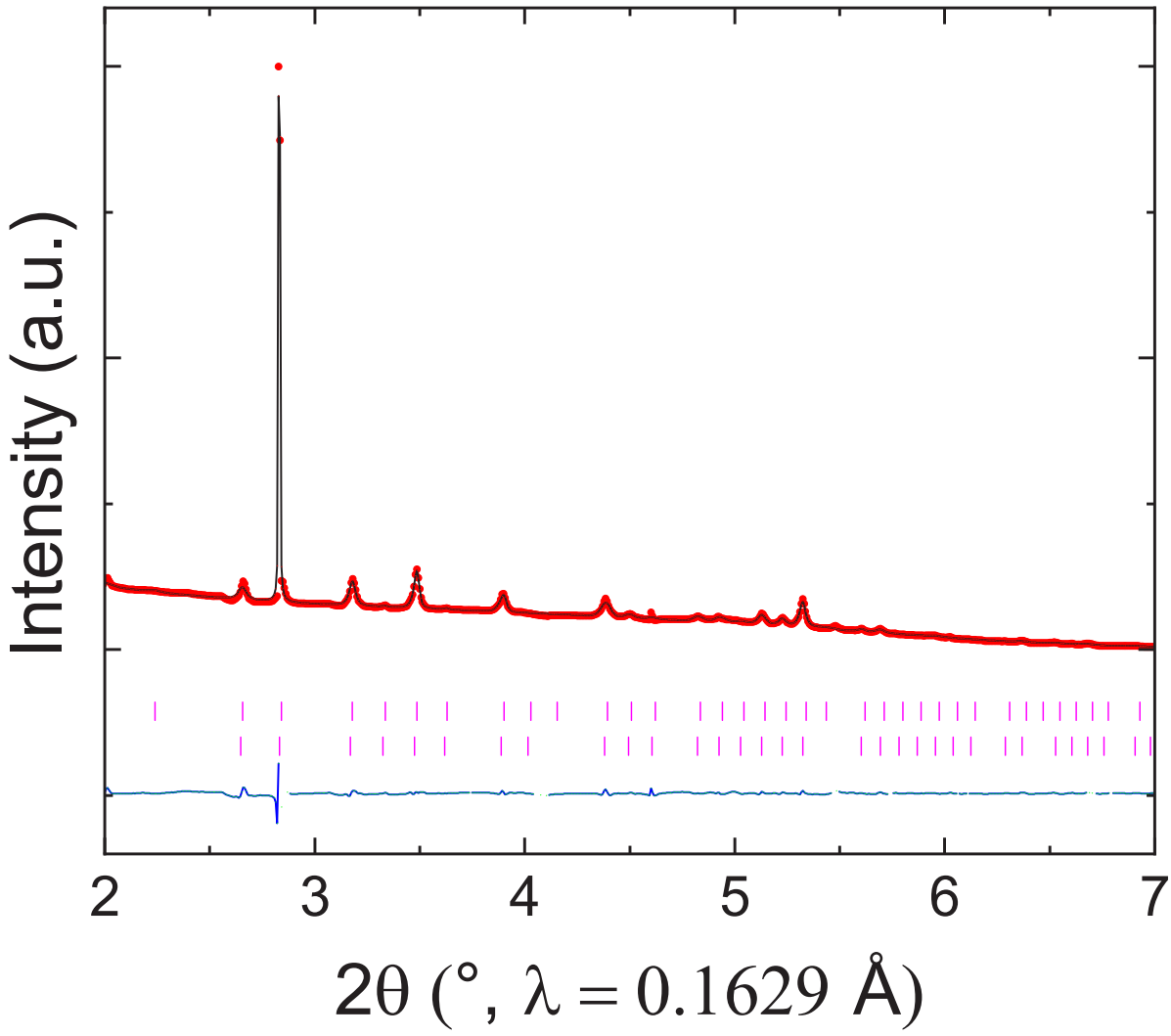

Fig S 12: Refinement for the high resolution XRD pattern obtained from the LLZO pellet. The refinement assumed both 220 and 230 space group with the identified lattice parameters.

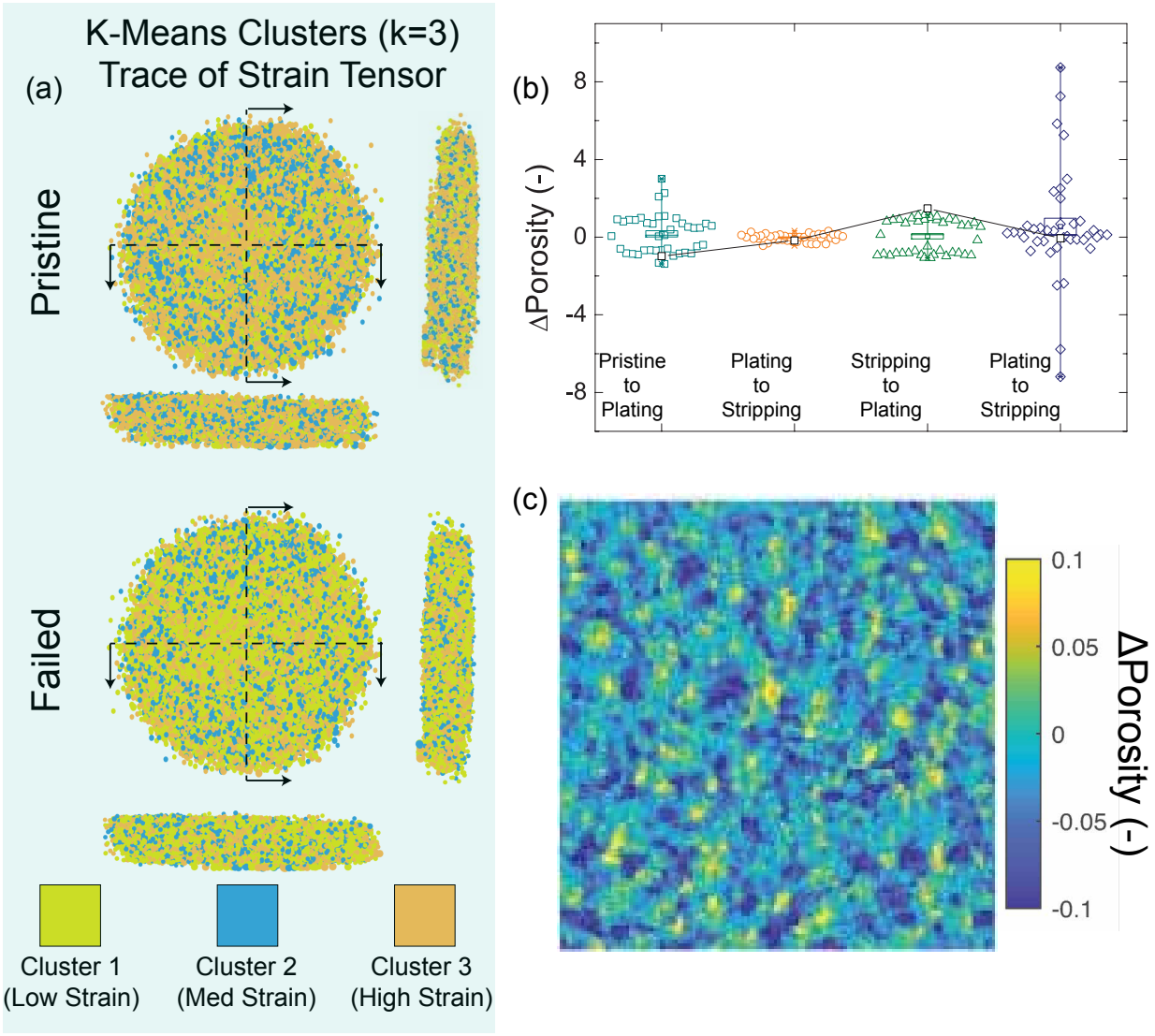

Fig S 13: Hydrostatic stress and microstructure evolution during cycling for additional sample. (a) Full pellet assessment for direction stress behavior using unsupervised machine learning algorithm, K-means. No preferential spatial distribution for the hydrostatic stress for individual grains is observed between the pristine and the failed sample. (b) Difference in porosity values tracked over the hot-spot and cold-spots for each step plotted as a box plot. Additionally, the average porosity difference over the entire pellet between each step is overlayed and connected by a solid line. As the sample undergoes degradation with cycling, the hot-/cold- neighborhoods clearly show very high variance in the porosity change compared to the bulk sample value. (c) Depth averaged Δ porosity values for identical sub-volume sizes taken at a hot spot region (right). The porosity difference is calculated between the pristine and the failed sample. The scale bar in the figure is 10 μm.

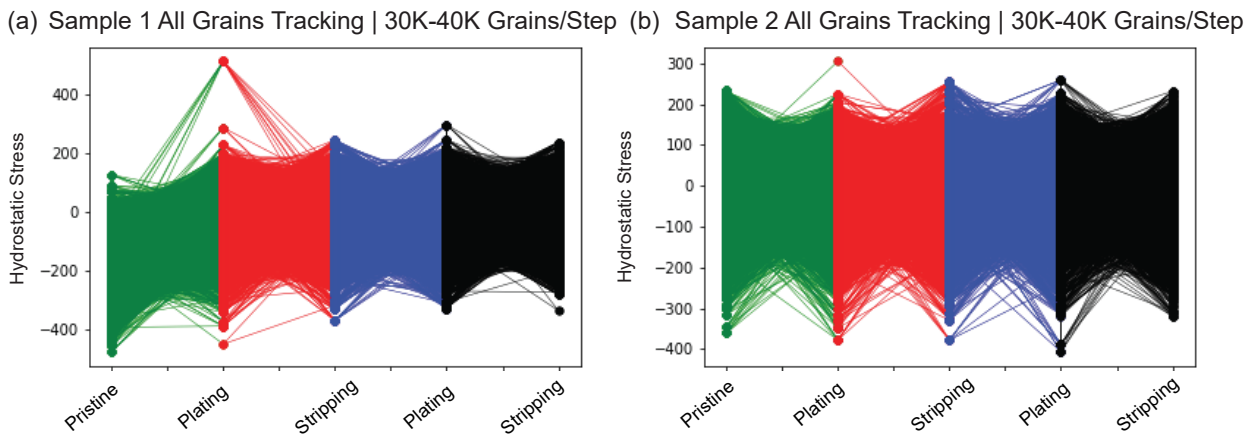

Fig S 14: Hydrostatic Stress Tracking for all grains of the two pellets (a-b) across the electrochemical steps. A majority of the grains do not show any deviation in the stress values as expected from the aggregate plots (Fig. 1c, S4a).

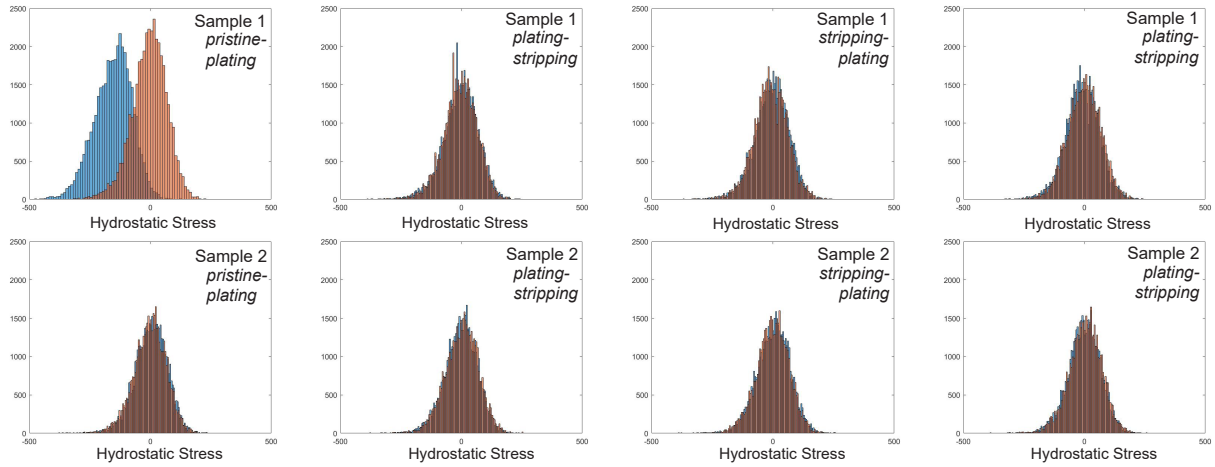

Fig S 15: Hydrostatic Stress Tracking for all grains of the two pellets (a-b) as histogram profiles plotted for two electrochemical steps. The blue curve is for the first state and the orange curve is for the second state. A majority of the grains do not show any deviation in the stress values as expected from the aggregate plots (Fig. 1c, S4a).

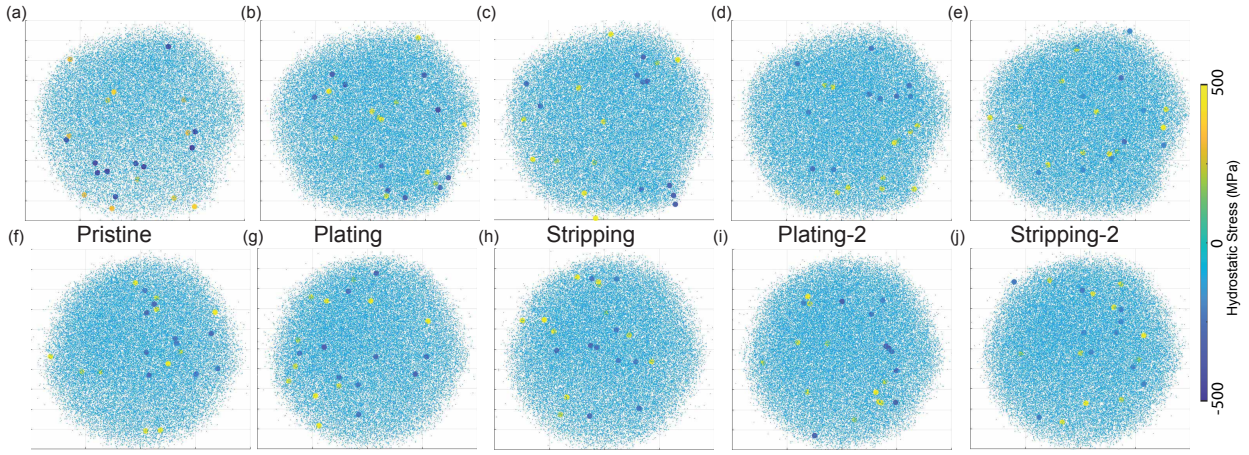

Fig S 16: Identification of hot-/cold- spots for LLZO across various stages of electrochemical cycling (a-e) for sample 1 and (f-j) for sample 2. Hot- and cold- spots are defined as ten grains with the highest and lowest hydrostatic stress in the measured pellet grain map and are depicted with larger scatter sizes. The color for the rest of the grains is merely for representation and does not signify any physical quantity.

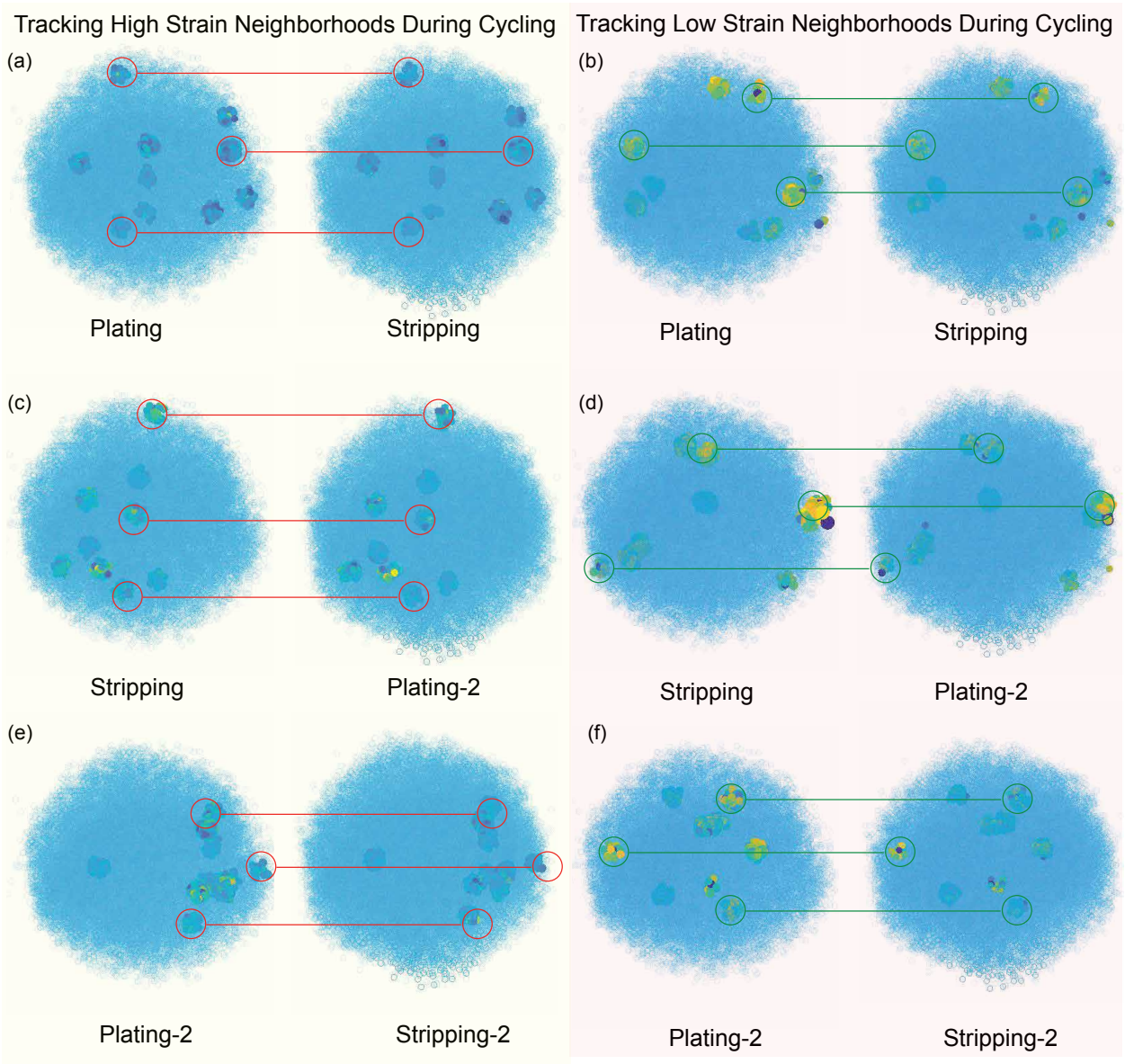

Fig S 17: Hydrostatic stress evolution during cycling. Tracking of high stress and low stress neighborhoods at different stages of cycling for sample 1. (a-b) Plating to stripping. (c-d) Stripping to Plating-2. (e-f) Plating-2 to Stripping-2.

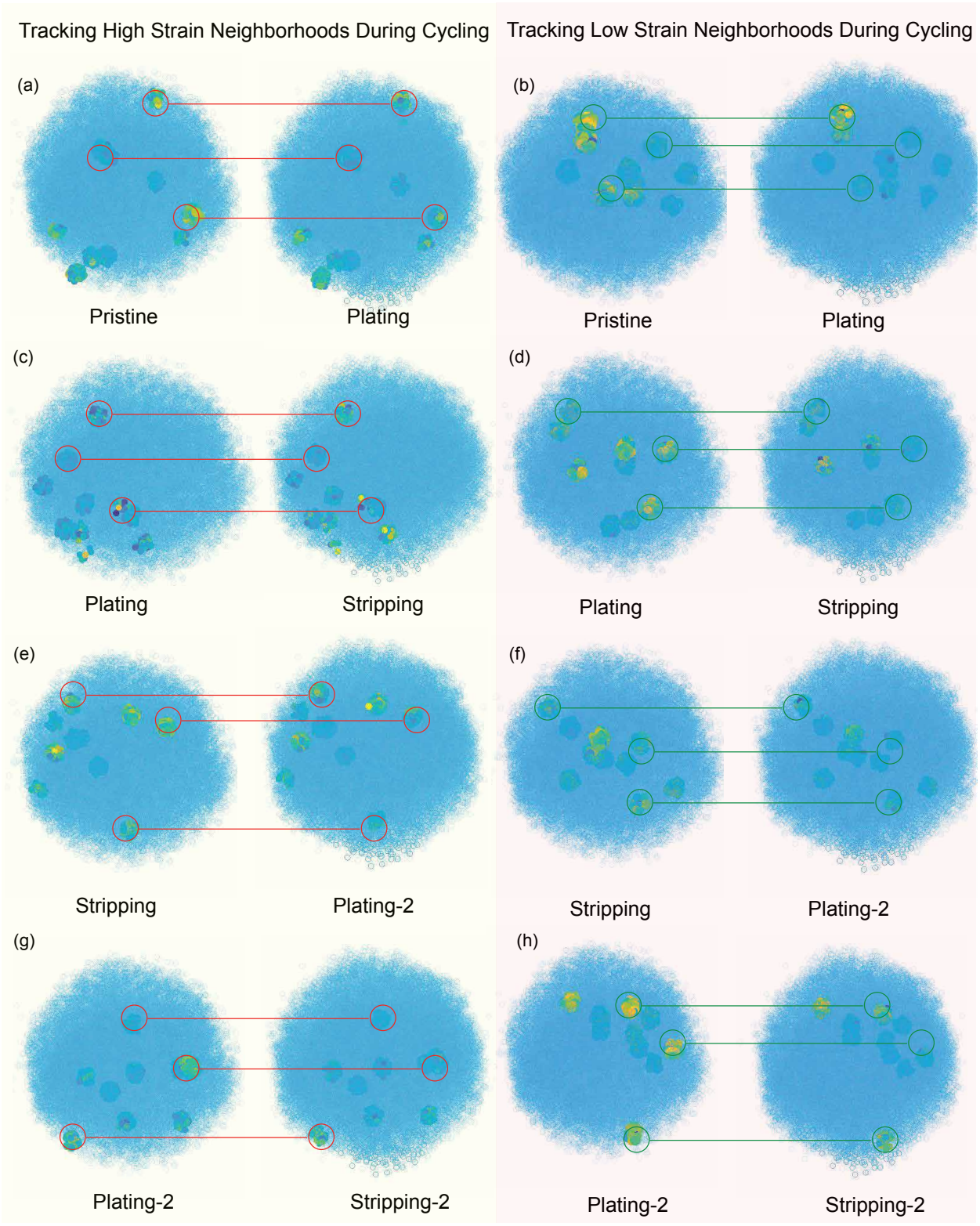

Fig S 18: Hydrostatic stress evolution during cycling. Tracking of high stress and low stress neighborhoods at different stages of cycling for sample 2. (a-b) Pristine to plating. (c-d) Plating to stripping. (e-f) Stripping to Plating-2. (g-h) Plating-2 to Stripping-2.

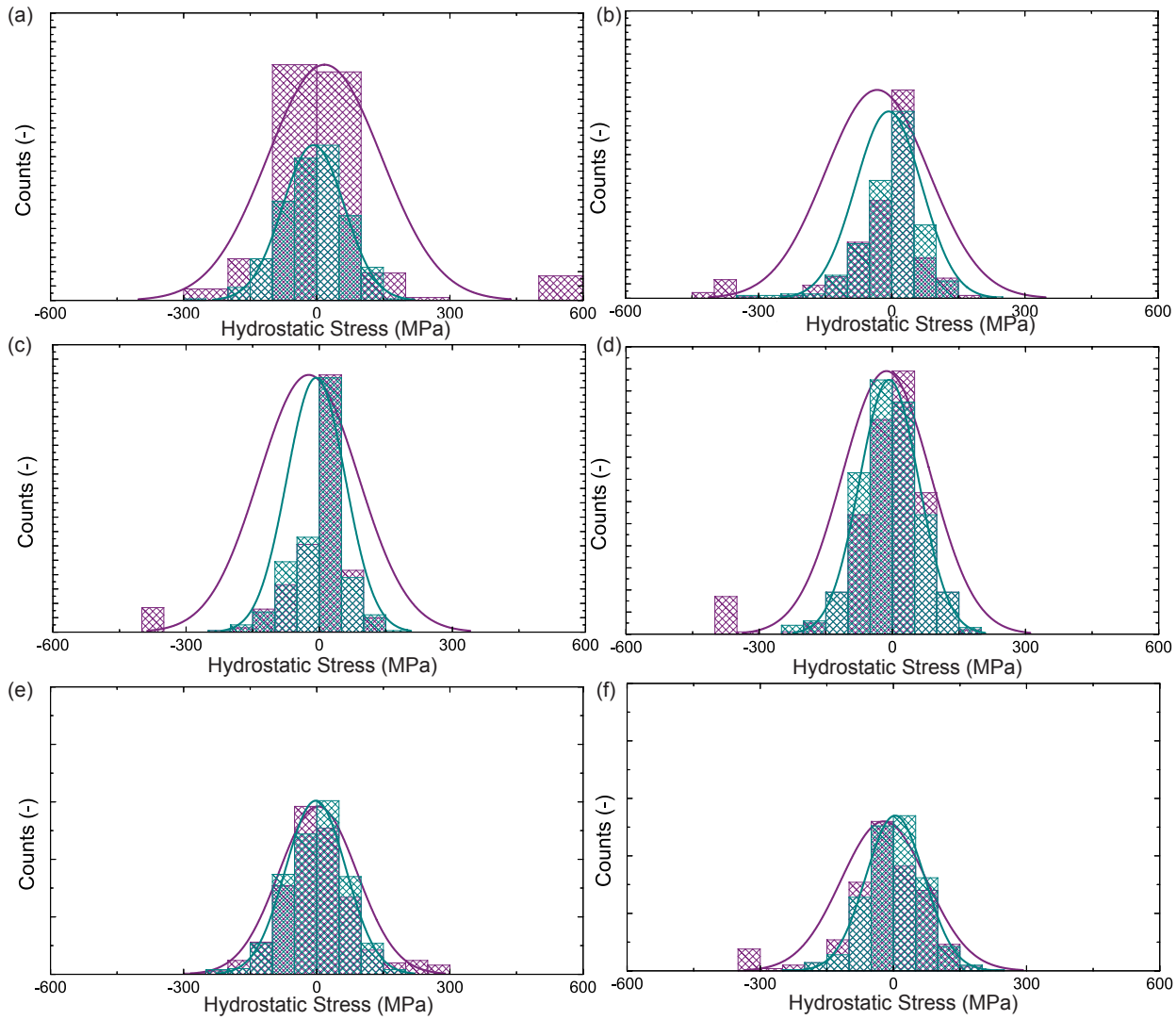

Fig S 19: Hydrostatic stress evolution during cycling. Tracking of high stress and low stress neighborhoods at different stages of cycling for sample 1 with the corresponding histograms and normal distribution fitting for the hydrostatic stress value for the grains in the identified neighborhood. (a-b) Plating to stripping. (c-d) Stripping to Plating-2. (e-f) Plating-2 to Stripping-2.

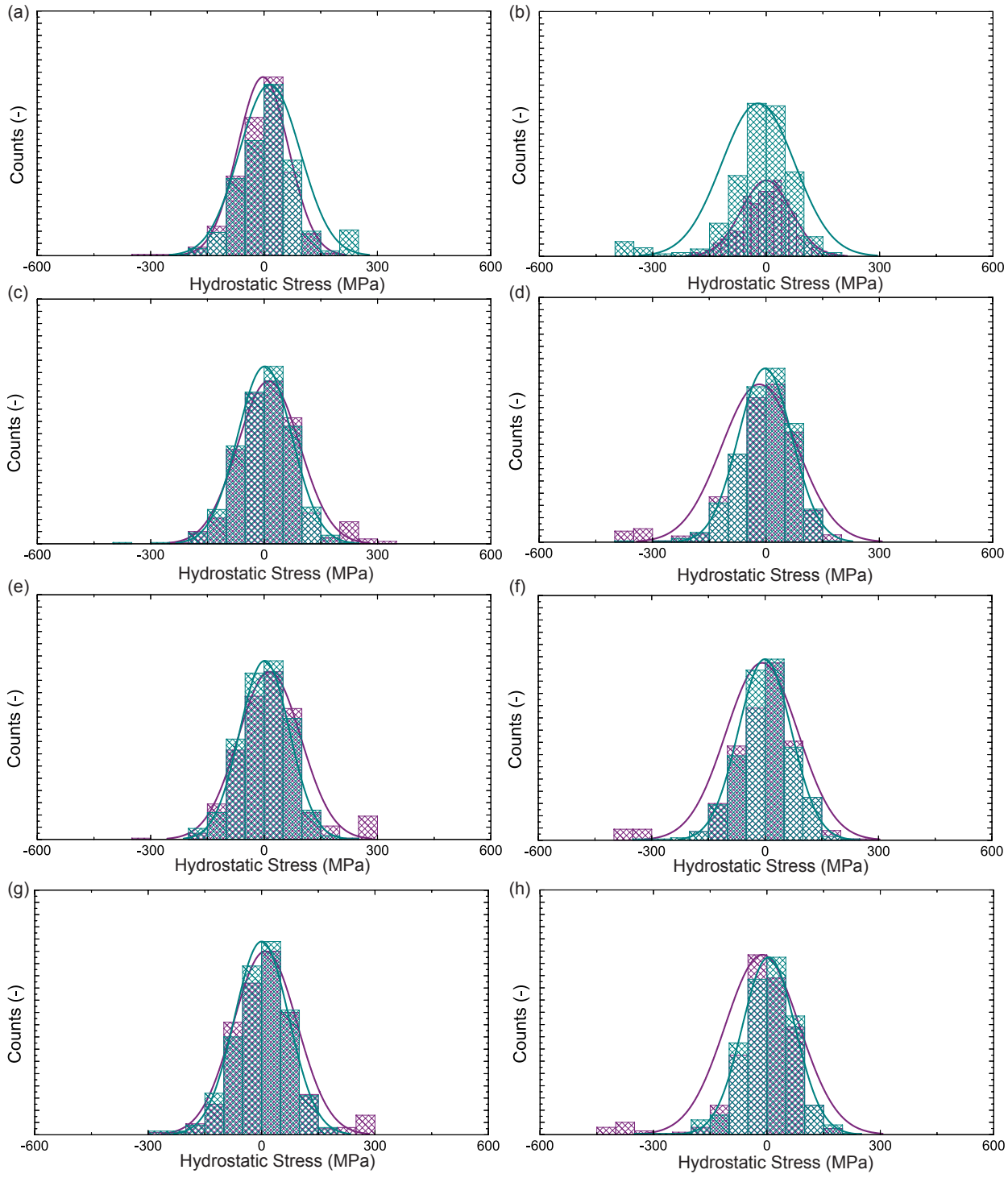

Fig S 20: Hydrostatic stress evolution during cycling. Tracking of high stress and low stress neighborhoods at different stages of cycling for sample 2 with the corresponding histograms and normal distribution fitting for the hydrostatic stress value for the grains in the identified neighborhood. (a-b) Pristine to plating. (c-d) Plating to stripping. (e-f) Stripping to Plating-2. (g-h) Plating-2 to Stripping-2.

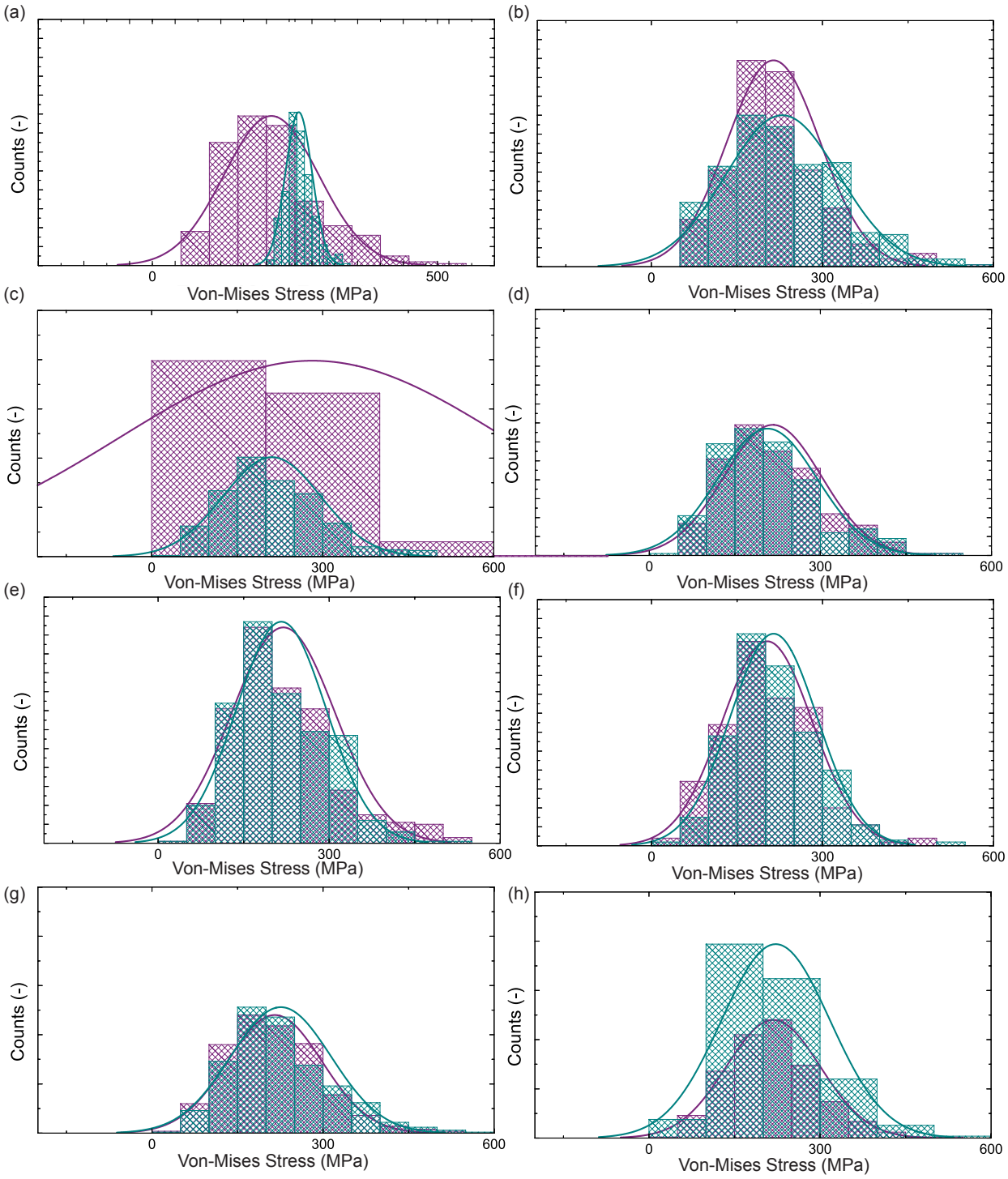

Fig S 21: Von-Mises stress evolution during cycling. Tracking of high stress and low stress neighborhoods at different stages of cycling for sample 1 with the corresponding histograms and normal distribution fitting for the hydrostatic stress value for the grains in the identified neighborhood. (a-b) Pristine to plating. (c-d) Plating to stripping. (e-f) Stripping to Plating-2. (g-h) Plating-2 to Stripping-2.

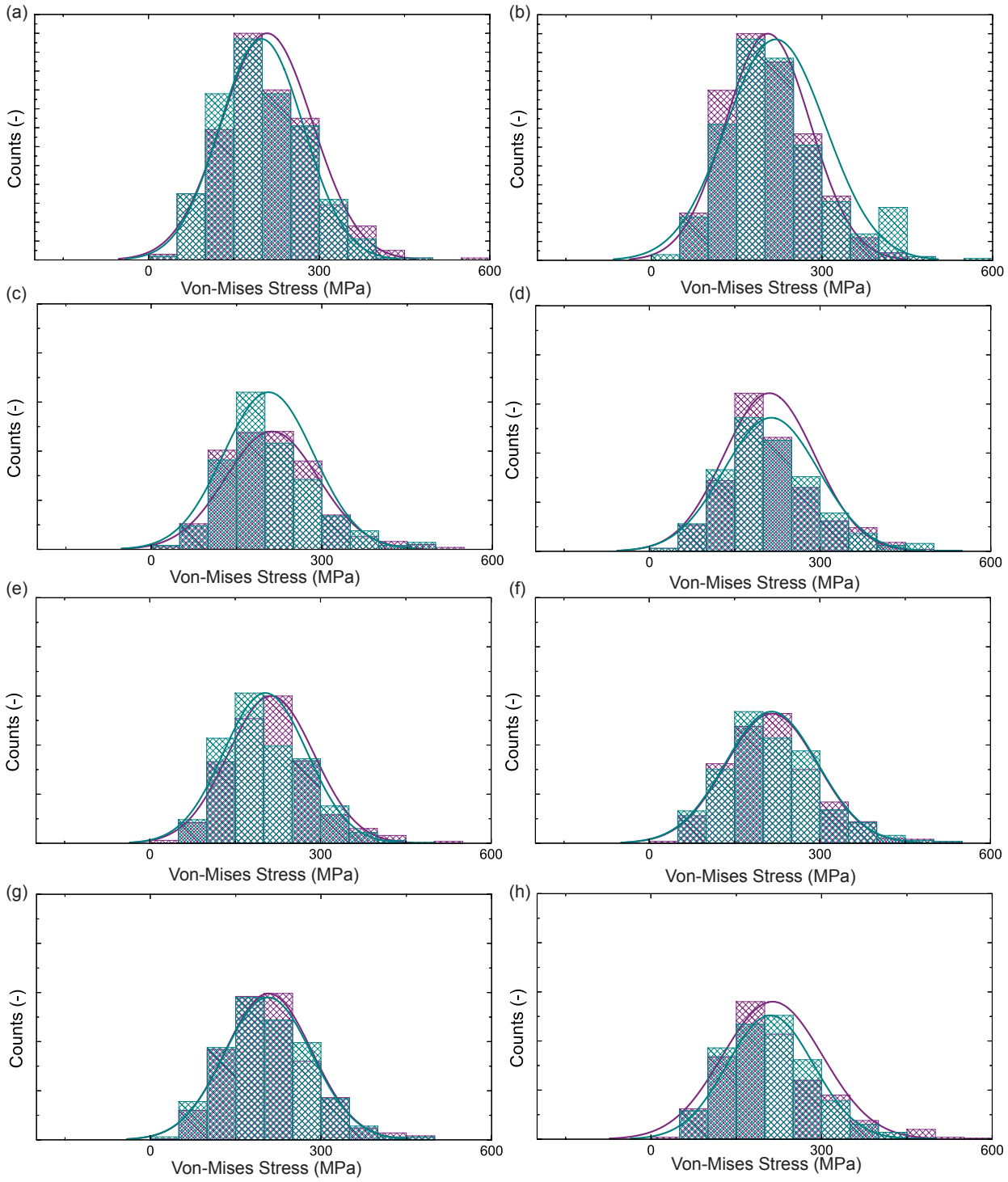

Fig S 22: Von-Mises stress evolution during cycling. Tracking of high stress and low stress neighborhoods at different stages of cycling for sample 2 with the corresponding histograms and normal distribution fitting for the hydrostatic stress value for the grains in the identified neighborhood. (a-b) Pristine to plating. (c-d) Plating to stripping. (e-f) Stripping to Plating-2. (g-h) Plating-2 to Stripping-2.

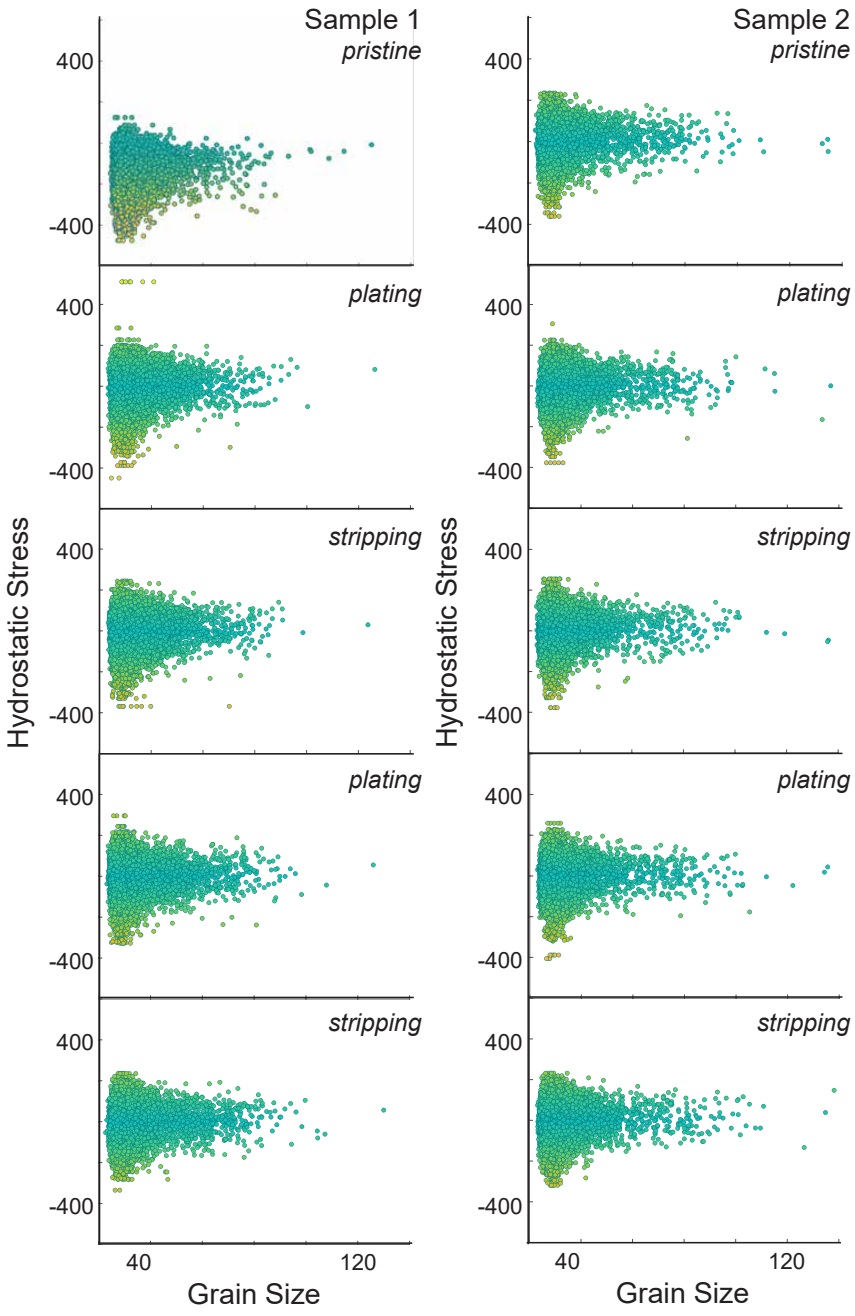

Fig S 23: Distribution of hydrostatic stress of individual grains for each step of electrochemical cycling for the two samples as a function of the estimated grain size. Typically, larger grains show relatively low stress values compared to the smaller grains.

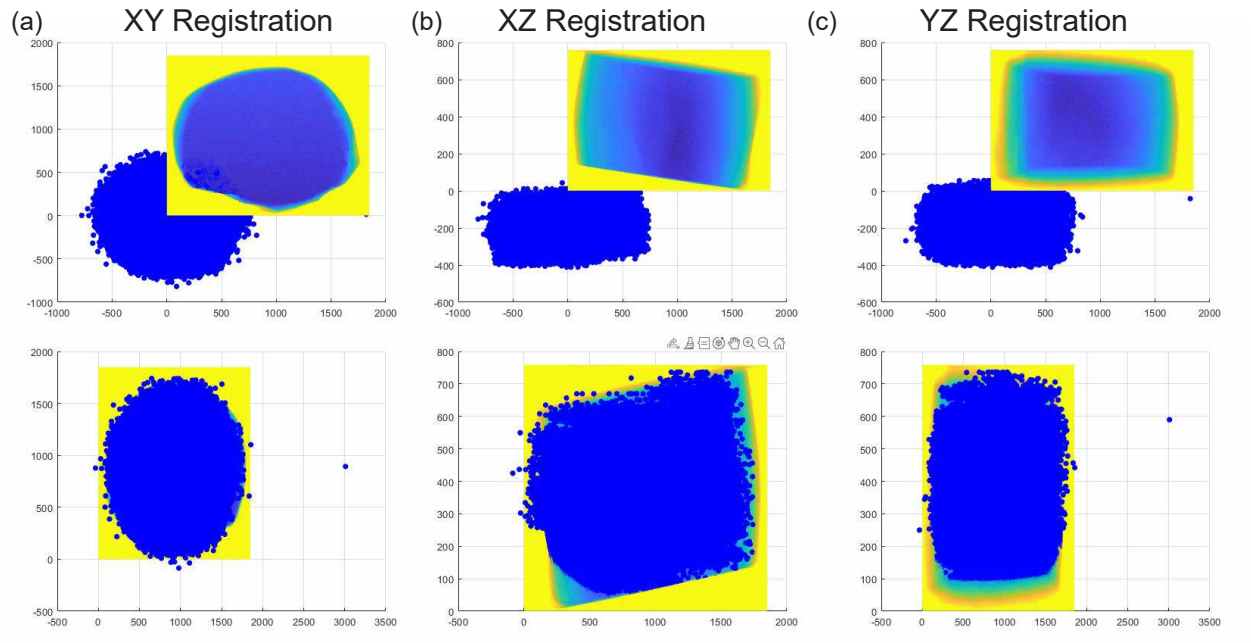

Fig S 24: Registration of the tomography and HEDM data sets. For each step, the grain map and tomography datasets were aligned through a series of translation and rotational transformations along the three planes: (a) XY, (b) XZ and (c) YZ. The registered data-sets were then used to extract the corresponding locations of hot-/cold- spots identified from the grain maps within the tomography data-set.

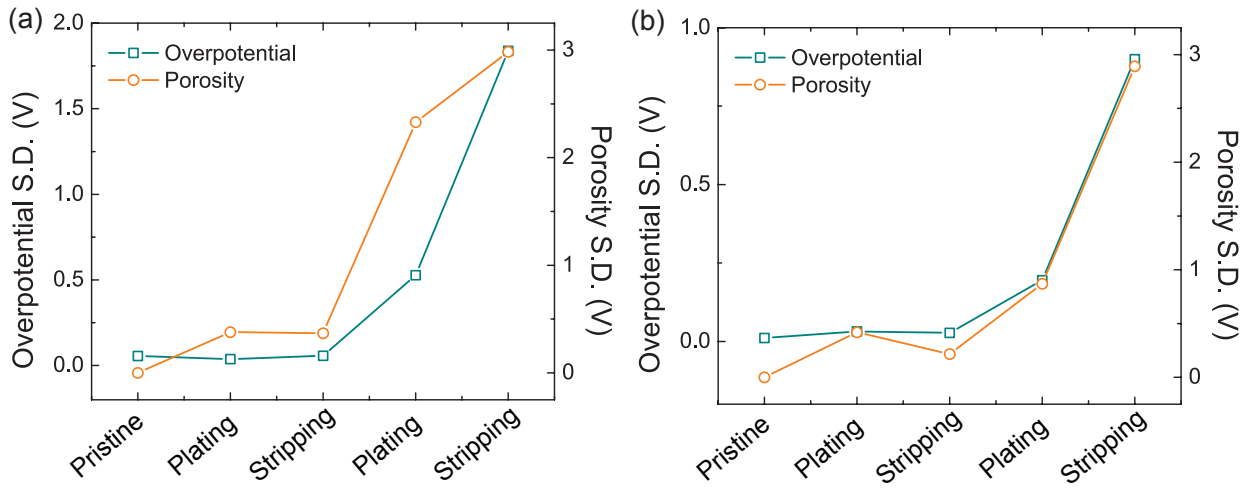

Fig S 25: Correlation between cell degradation and the local change in porosity. Standard deviation for the observed Li plating/stripping overpotential during each half-cycle and the standard deviation of the local porosity of the hot-spots identified are plotted for (a) Sample 1 and (b) Sample 2. Strong correlation between the two data-sets are observed.

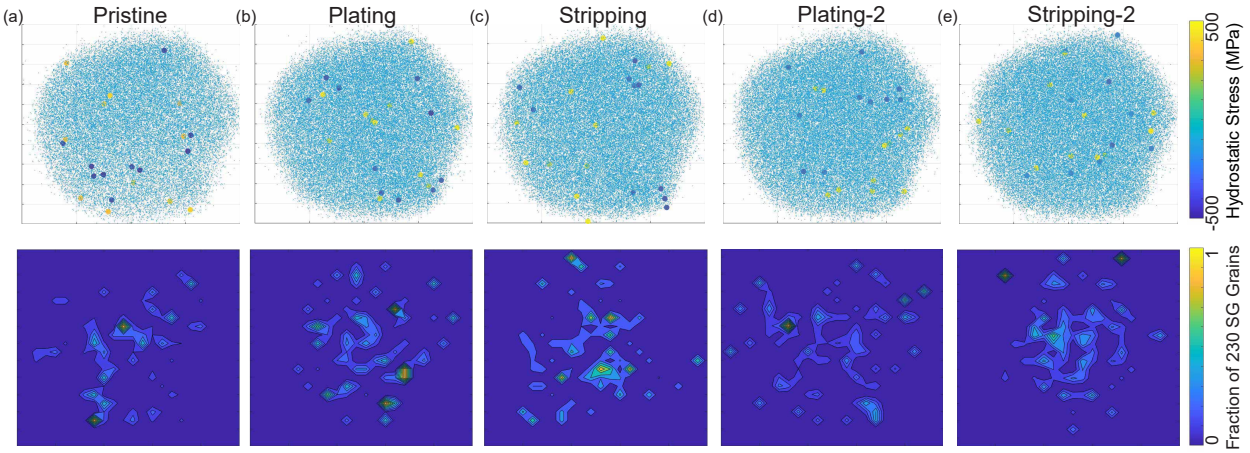

Fig S 26: Correlating FF-HEDM and Tomography datasets (a) Cross-sectionally averaged map within the bulk of the solid electrolyte with hot-/cold- spots identified with filled markers while the rest of the grains are hollow markers. Below this maps, are the spatial map of 230 space group grain maps. The grain maps are plotted as contour plots of the local number of grains in 230 space group compared to 220 space group. A correlation between the regions of higher 230 grains and the hot-spots can be seen. The results here are plotted for Sample 1.

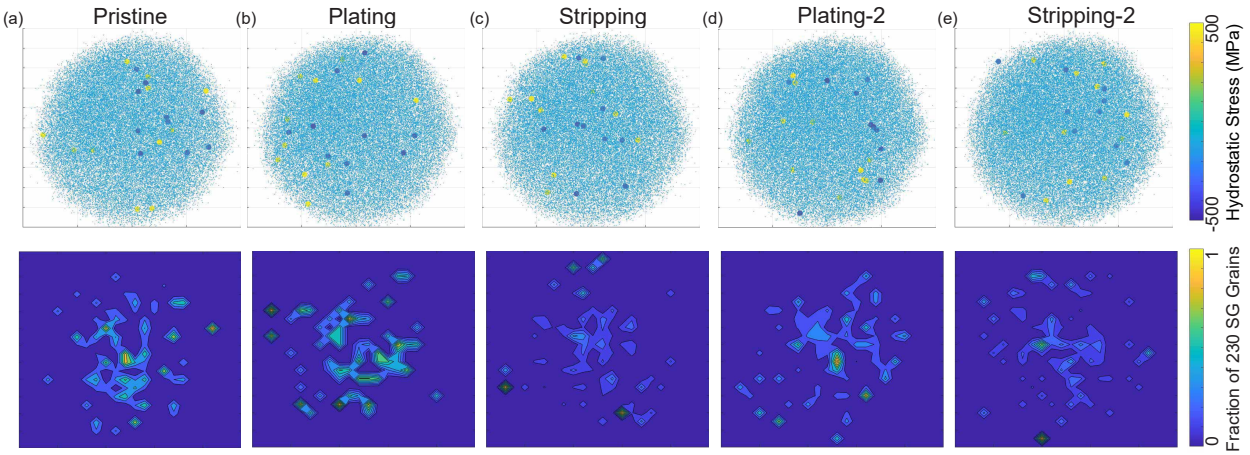

Fig S 27: Correlating FF-HEDM and Tomography datasets (a) Cross-sectionally averaged map within the bulk of the solid electrolyte with hot-/cold- spots identified with filled markers while the rest of the grains are hollow markers. Below this maps, are the spatial map of 230 space group grain maps. The grain maps are plotted as contour plots of the local number of grains in 230 space group compared to 220 space group. A correlation between the regions of higher 230 grains and the hot-spots can be seen. The results here are plotted for Sample 2.

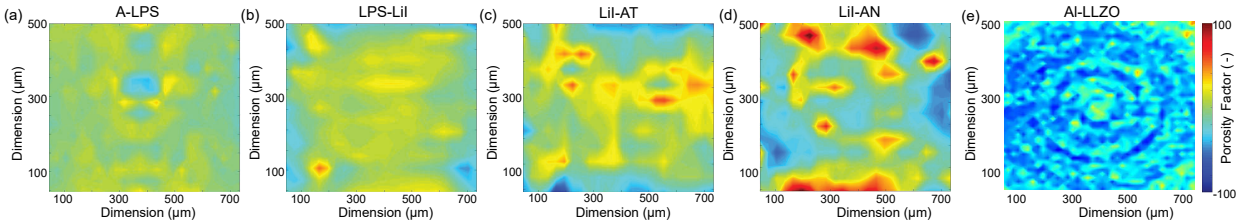

Fig S 28: Porosity factors for various solid electrolytes. Porosity factor is defined as the ratio of local porosity identified for a small sub-volume to the average porosity of the pellet. Porosity maps are calculated across the in-plane section in the electrolyte which is normal to the applied electric field and represent the horizontal cross section of the pellet. Through plane is parallel to the applied electric field and represents the vertical cross section of the pellet. Porosity factor variation in through-plane direction for A–LPS, LPS:0.5LiI, LiI–AT, LiI—AN and Al-LLZO (a)-(e).